Improved simulation of drop dynamics in a shear flow at low Reynolds and capillary number

I. Halliday, R. Law, C. M. Care, and A. Hollis

Materials and Engineering Research Institute, Sheffield Hallam University, Howard Street, Sheffield S1 1WB, United Kingdom

The simulation of multicomponent fluids at low Reynolds number and low capillary number is of interest in a variety of applications such as the modeling of venule scale blood flow and microfluidics; however, such simulations are computationally demanding. An improved multicomponent lattice Boltzmann scheme, designed to represent interfaces in the continuum approximation, is presented and shown (i) significantly to reduce common algorithmic artifacts and (ii) to recover full Galilean invariance. The method is used to model drop dynamics in shear flow in two dimensions where it recovers correct results over a range of Reynolds and capillary number greater than that which may be addressed with previous methods.

I. INTRODUCTION

Many multicomponent flows are conveniently modeled using the lattice Boltzmann (LB) method; microfluidic multicomponent flows are a relevant example. The latter are characterized as complex, incompressible flows at small Reynolds number, Re, and small capillary number, Ca. Multiple blood cells in venule-scale flows have also been represented with LB as immiscible drops (a traditional device) [1,2]; such flows have $Re \sim 1$ and may be simulated using values of $Ca \sim 2.0$. Simulation by means of LB, of such non-Brownian colloidal systems is subject of this work. Traditional computational fluid dynamics has also, of course, been applied in similar situations; recently Jadhav *et al.* have used the immersed boundary method to three-dimensional simulations of leukocyte rolling [3] and, in the wider context, Esmaeeli and Tryggvason have presented simulations of bubbles at low Re; see Ref. [4] and references therein and Sankaranarayanan *et al.* [5] have produced a comparative study of LB and front-tracking finite-difference methods for bubble simulations.

The several multicomponent LB methods may be distinguished by the different ways in which they impose a fluid-fluid interface. Illustrative references are Refs. [6–10]. See also Refs. [12,13] for a survey of the methods' relative advantages and applications. In problems where the kinematics of phase separation feature, Swift's method [6,8], based as it is upon the Cahn-Hilliard theory, represents an appropriate choice of LB interface algorithm. Here, however, we aim to address only completely immiscible mixtures in a continuum approximation, in which interfaces are assumed to be very narrow and unstructured. Computational resources or physical accuracy may also impose similar requirements and restrict choice of interface algorithm to a type pioneered by Gunstensen *et al.* [9] and later modified by Lishchuk *et al.* [10]. The model presented and applied here is based on the latter. As such, its interface is based on the stress boundary conditions which apply on the boundary between completely separated fluids, imposed through a body force acting in the fluid; an idea first introduced in the context of interfacial tension by Brackbill, Kothe, and Zemach in 1992 [11].

Lishchuk's method (i) produces narrow interfaces with small microcurrents (i.e., spurious velocities) [12], (ii) has an independently adjustable interfacial tension, (iii) is conveniently direct, and (iv) can produce interfacial tensions larger than Gunstensen's method [9]. The key feature of the Lishchuk method is that, in order to impose surface tension, it impresses a curvature-dependent force in what is effectively a single fluid. However, both methods have a problem reaching low Ca and drop Reynolds number, Re_d (defined below), giving rise to a tendency for drops to facet as Ca and Re_d decrease; i.e., lengths of interface with zero curvature form parallel to lattice directions. Faceting is associated with a reduced drop advection and hence Galilean invariance. In this paper we introduce a set of remedies.

(1) Accuracy of the interface forcing: we use the method of Guo *et al.* [14], to develop an interface forcing with reduced discrete lattice effects and explicit enforcement of conservation of global momentum.

(2) Accuracy of key numerical derivatives: we use $O(4)$ accurate derivatives (in mesh-spacing) for a more distributed forcing around the sharp phase-field boundary (interface).

(3) Explicit consideration of the kinematic condition of mutual impenetrability of fluids at an interface.

In Sec. II the problem is further discussed. In Sec. III we summarize relevant background issues relating to our foundation model, defined in Ref. [10]. In Sec. IV we expand on the innovations identified above and in Sec. V, assess them for low Re and low Ca deformable drop lift calculations. We present conclusions in Sec. VI.

Our recent *N*-immiscible component model [1,2] could be modified along lines identical to those discussed in this paper. However, for simplicity, in this paper we address only two, completely immiscible fluid components, designated red (drop) and blue (embedding fluid). Throughout we use the standard notation used in Ref. [10], defining only new or modified parameters. While we work in two dimensions, all the modifications we introduce generalize self-evidently into three dimensions. We denote the shear and kinematic viscosity η and ν, respectively. The drops we consider have radii R and surface tension α. Their flow environment is characterized by a velocity U_0 and/or a shear rate $\dot{\gamma}$.

II. THE PROBLEM

The objective of the work reported in this paper, to which the present section provides background, is to modify Lishchuk's method [10], to improve the representation of completely immiscible stiff drops in slow flow.

Consider the simulation of the flow of high volume fraction, non-Brownian colloids in complex, internal geometry. At some positions in the geometry, the flow velocity is likely to be small. Now suppose we need to simulate stiff drops. We therefore require a small capillary number, Ca and must expect to encounter a small drop Reynolds' number, Re_d,

$$Ca \equiv \frac{\text{viscous deforming stress}}{\text{interfacial restoring stress}} = \frac{\rho \nu \dot{\gamma} R}{\alpha}, \qquad (1)$$

$$Re_d \equiv \frac{\text{local inertial effects}}{\text{local viscous effects}} = \frac{\dot{\gamma} R^2}{\nu}. \qquad (2)$$

LB fluids are described by the Navier-Stokes and continuity equations only for restricted Mach number $M \equiv U_0/c$ [12]; usually $M \leqslant 0.1$ is required. The fact that LB models have a small speed of sound $c \sim O(1)$ therefore limits the value of U_0. It follows that low Ca, low Re_d must be achieved using large α and limiting $\dot{\gamma}$. But a velocity which is too small is also a problem. In the interfacial region of multicomponent LBs, there exist unphysical velocity field fluctuations, or microcurrents, generated by the interface algorithm. To obscure these, one approach to target Re_d and Ca is to limit length scale and maintain the characteristic velocity. Where length scale is limited, narrow interfaces are necessary to avoid introducing a length scale which may conflict with that of the flow problem, e.g., Ref. [1].

The above requirements translate to a need for (i) a sharp phase-field boundary, (ii) large surface tensions, and (iii) a small LB microcurrent. While Lishchuk's method [10] facilitates (i)–(iii), as $Re \rightarrow 0$ a lack of Galilean invariance arises as droplets pin on the lattice.

Wagner [15] has pointed out the origin of the microcurrents in multicomponent LBs [15]; imperfect correlation between an interface-producing force and the dynamics of the phase index, or color label, ρ^N [see Eq. (9) and Sec. III] means fluid is kept in constant motion near the interface. Enhanced consistency between the interface-inducing force and the ρ^N field decreases the microcurrent. These considerations may be set in context as follows.

In our core algorithm of Ref. [10], the force applied to create the interface (discussed in Sec. III) is defined in terms of derivatives of ρ^N [see Eq. (10)]. Sharp interfaces lead to numerical error in the calculation of these spatial gradients of ρ^N, resulting in anisotropic forcing over the drop perimeter. Microcurrents and a small, damped shape fluctuation ensue. By distributing the interface, the accuracy of numerical gradients may be improved, making the interface forcing more isotropic. Figure 1 shows data obtained from simulations which use an idealized phase field,
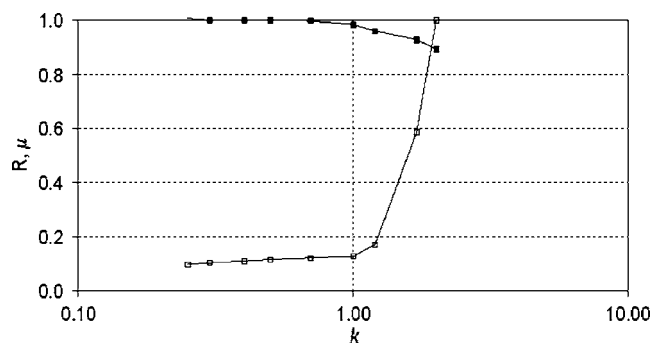
FIG. 1. Data from the multicomponent LB algorithm of Ref. [10]. Normalized, whole-lattice microcurrent activity, μ (open squares) and surface tension isotropy, R (solid squares) for a range of interface thickness parameter, k. Ratio R is obtained as described in Sec. II. These data were obtained for a neutrally buoyant drop, initial radius 15 lattice units, placed on a 75×75 lattice, with collision parameter $\tau = 1$.

$$\rho^N(x,y) = \tanh[k\sqrt{(x-x_0)^2 + (y-y_0)^2}], \qquad (3)$$

in which interface thickness parameter, k, has been varied. See the figure caption for simulation data. With $k \approx 2.4$ (typical of numerical color segregation) the interface width is less than two lattice spacings. Decreasing k distributes the interface and improves numerical derivatives of ρ^N. The interface-inducing force integrated along a radial path crossing the interface measures interfacial tension [10]. A numerical integral was obtained for cuts at drop perimeter locations at (i) 0 rad and (ii) $\pi/4$ rad. R is the ratio of this force integral in (i) to that in (ii). In Fig. 1, as k decreases, $R \rightarrow 1$ and the total microcurrent activity falls. The latter was measured as the lattice sum of the velocity modulus, $\sqrt{u_x^2 + u_y^2}$, normalized to its value for $k = 2.4$. A more accurate interface-generating force appears to reduce microcurrents. In the present context, accuracy relates to the quality of numerical derivatives.

Next consider an immiscible drop embedded in a fluid, moving with uniform velocity U_0. In any multicomponent LB the interfacial microcurrent increases in proportion to surface tension, α. It also varies weakly with fluid viscosity, which we ignore; the latter limitation does not affect our observations. As U_0 decreases, the speed at which the drop advects, U_d, approaches the value which characterizes microcurrent activity and there is a loss of advection for the drop. This is more fully discussed in Sec. V C. Figure 2 shows the results of advection tests using our original algorithm of Ref. [10], outlined in Sec. III. A drop embedded in uniform flow is characterized by ordinal value $U_d/U_0 = 1$, a completely trapped drop by $U_d/U_0 = 0$. These data were compiled for a range of α and U_0. All data lie about the solid line inserted in Fig. 2 which is a grid search optimized fit to the data using an expression of the form $\tanh[a(U_d/U_0) - b]$. It was found that $a = 0.049$. From Fig. 2 it is clear that for $U_0/\alpha \leqslant 0.1$ there results a progressive loss of advection in our basic algorithm of Ref. [10]. Note that the results of Fig. 2 do not set a characteristic minimum on the value of quotient U_0/α; microcurrent activity is, recall, slightly influenced by fluid viscosity.
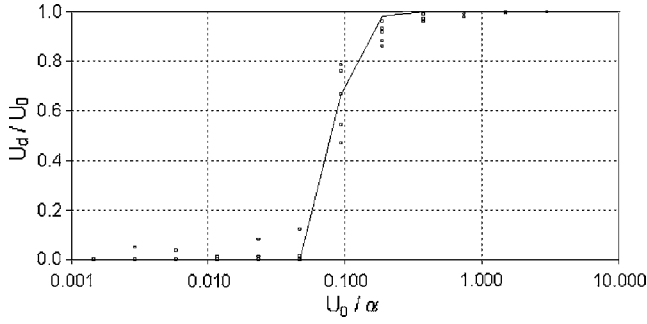
FIG. 2. Original LB algorithm of Ref. [10]. The final advection speed, U_d, of an infinite chain of red drops, surface tension α, responding to far-field motion $(U_0,0)$ is normalized to U_0 and plotted as a function of ratio U_0/α. These data were obtained for a neutrally buoyant drop, initial radius 15 lattice units, placed on a 75×75 lattice, for a range of values of boundary velocities, U_0 and interfacial tensions α. The solid line is a grid-search optimized tanh profile fit to the data. As the surface tension increases for fixed advection velocity, the drop stalls.

The simple case of a lack of Galilean invariance expressed in Fig. 2, is compounded in what we shall term a general notion of Galilean invariance. Consider again the immiscible drop. Its motion is a response to the accumulation of interfacial stresses. However, in all multicomponent LB, interface is created by a perturbation which degrades the hydrodynamic stresses and, therefore, the drop's dynamics. Since this effect becomes more noticeable when stresses are relatively small, it is evident that we need a refined multicomponent LB model first for the small Re, small Ca regime. In the present context, the benefits of our improved method arise in part because the interface perturbation better respects viscous stress. Results show general loss of Galilean invariance properties at low Re_d, low Ca, assessed by means of lift simulations, are improved by the innovations introduced in Sec. IV without compromising on the length scale of the interface.

We stress that, for small Ca, large Re_d, the basic model outlined in the next section exhibits fewer problems. It is upon slow, $Re_d \sim 1$, surface-tension dominated, Ca<2, flow that the reported innovations focus.

III. MULTICOMPONENT LATTICE BOLTZMANN IN THE CONTINUUM APPROXIMATION

The work reported here and in Ref. [10] is based upon the popular single component LB variant widely designated the LBGK model, due to Qian *et al.* [16], to which a source term, $\phi_i(\mathbf{r})$ is added, to create interfacial tension,

$$f_i(\mathbf{r} + \mathbf{c}_i, t + 1) = f_i(\mathbf{r},t) - \frac{1}{\tau}[f_i(\mathbf{r},t) - f_i^0(\rho, \rho\mathbf{u})] + \phi_i(\mathbf{r}).$$

$$(4)$$

Here $0 \leq 1/\tau \leq 2$ is a selectable parameter which controls the viscosity of the underlying fluid. The method's primary quantity, momentum distribution function f_i, is fully discussed in Ref. [12]. Note that Eq. (4) assumes unit time step. It refers to those lattice links $\mathbf{c}_i$ and weights t_p defined in Table I. The solution to Eq. (4), f_i, generates isothermal observables ρ and $\mathbf{u}$,

$$\rho \equiv \sum_i f_i, \quad \mathbf{u} \equiv \frac{1}{\rho}\sum_i f_i \mathbf{c}_i, \quad (5)$$

for an isothermal equilibrium $f_i^0(\rho, \mathbf{u})$,

$$f_i^0(\rho, \mathbf{u}) = t_p \rho \left[1 + 3\mathbf{u} \cdot \mathbf{c}_i + \frac{9}{2}(\mathbf{u} \cdot \mathbf{c_i})^2 - \frac{3}{2}u^2\right]. \quad (6)$$

For a constant source term, ϕ_i, Chapman-Enskog analysis [12] leads to modified Navier-Stokes equations [17,10],

$$\frac{\partial}{\partial t}\rho u_\alpha + \frac{\partial}{\partial x_\beta}\rho u_\beta u_\alpha = -\frac{\partial}{\partial x_\alpha}\rho + \frac{\partial}{\partial x_\beta}\frac{\partial}{\partial x_\beta}(2\rho\nu S_{\alpha\beta}) + \mathbf{F}_\alpha,$$

$$(7)$$

where $\nu \equiv \frac{1}{6}(2\tau - 1)$, $S_{\alpha\beta}$ is the strain rate tensor and the source term ϕ_i is responsible for a constant body force,

$$\mathbf{F} = \sum_i \phi_i \mathbf{c}_i. \quad (8)$$

Note, the summation convention on repeated greek subscripts applies in Eq. (7). For present purposes, the body force needs to contain spatial variation, $\mathbf{F} \rightarrow \mathbf{F}(\mathbf{r})$. This necessitates spatial variation in $\phi_i(\mathbf{r})$ which, in turn, complicates the derivation of Eq. (7) above. The solution given by Guo *et al.* to this problem, which we utilize in Sec. IV, requires a more complicated relationship between $\mathbf{F}(\mathbf{r})$ and $\phi_i(\mathbf{r})$ than that given in Eq. (8) and a redefinition of $\mathbf{u}$.

In order to distinguish between immiscible lattice fluids, our multicomponent LB uses a phase field based upon the densities of red and blue fluids present at a node. Following the notation of Ref. [10], we define a component index, or phase field, $\rho^N(\mathbf{r})$:

$$\rho^N(\mathbf{r},t) \equiv \left(\frac{\rho_R(\mathbf{r},t) - \rho_B(\mathbf{r},t)}{\rho_R(\mathbf{r},t) + \rho_B(\mathbf{r},t)}\right), \quad (9)$$

where $-1 \leq \rho^N(\mathbf{r}) \leq 1$. Note that ρ^N varies in time only

TABLE I. Definition of the D2Q9 simulation lattice link vectors, $\mathbf{c}_i$.

i	0 (rest)	1	2	3	4	5	6	7	8
t_p	4/9	1/9	1/36	1/9	1/36	1/9	1/36	1/9	1/36
c_{ix}	0	1	1	0	−1	−1	−1	0	1
c_{iy}	0	0	1	1	1	0	−1	−1	−1

through time dependence in $\rho_R(\mathbf{r},t)$ and $\rho_B(\mathbf{r},t)$. Red and blue fluids mix under the LB propagation step [12]; this defines the interfacial region. The two fluids are then segregated numerically [9].

The quantity $\mathbf{F}(\mathbf{r})$ is defined in terms of the gradients of $\rho^N(\mathbf{r})$. To achieve a cross-interfacial pressure step proportional to the local curvature in ρ^N, K, we take

$$\mathbf{F}(\mathbf{r}) \equiv \tfrac{1}{2}\alpha K \boldsymbol{\nabla} \rho^N, \qquad (10)$$

with α surface tension. Note that $\mathbf{F}(\mathbf{r})$ has also no explicit time dependence and that the right-hand side of Eq. (10) vanishes for constant ρ^N. The cumulative effect of the force [in Eq. (10)] produces a pressure step across the interfacial region. Assuming K to be locally constant, the local pressure step is obtained as the line integral of $\mathbf{F}(\mathbf{r})$ between the terminal points, A and B, of a short, normal path,

$$\Delta P = \tfrac{1}{2}\alpha K[\rho^N(B) - \rho^N(A)] = \alpha K. \qquad (11)$$

Note that A and B are embedded in the blue and red fluids, respectively, and so that $\rho^N(A) = -\rho^N(B) = 1$. Using the negative of a normalized color gradient as the interface normal, $\hat{\mathbf{n}}$, interface curvature K is obtained from the surface gradient,

$$K = n_x n_y \left(\frac{\partial}{\partial y} n_x + \frac{\partial}{\partial x} n_y \right) - n_x^2 \frac{\partial}{\partial y} n_y - n_y^2 \frac{\partial}{\partial x} n_x, \qquad (12)$$

where $\hat{\mathbf{n}} \equiv \boldsymbol{\nabla}\rho^N / |\boldsymbol{\nabla}\rho^N|$. It is important to note that the evaluation of K involves numerical second derivatives of ρ^N.

For the body-force defined in Eq. (10), arguments are presented in Ref. [10] which yield a source term, ϕ_i of the form

$$\phi_i(\mathbf{r}) \equiv \tfrac{3}{2} t_p \alpha K (\boldsymbol{\nabla}\rho^N) \cdot \mathbf{c}_i, \qquad (13)$$

which result, we stress, is improved in Sec. IV. Note that the constant $3/2$ which appears in Eq. (13) has units of (lattice velocity)$^{-4}$(lattice distance)$^{-1}$ [10].

In order to achieve narrow interfaces, numerical demixing of red and blue fluids at an interface is necessary [9,18]. The interface algorithm outlined in the current section is based upon a variable force applied locally in a single fluid, to eliminate curvature in a phase field. This accurately represents interface dynamics (stress conditions) [10]. But the extent to which the kinematic condition of mutual impenetrability is implicit is unclear; the fact that there is a single sum fluid means that the combined momentum of the mixture of fluids is continuous across an interfacial region but the velocities of the red and blue fluids may not be easily defined close to the interface.

IV. IMPROVED MODEL

We describe a number of modifications to the algorithm outlined above. In summary,

(1) The source term, ϕ_i, in Eq. (4) is modified more accurately to recover the required interface force in Eq. (7); this is achieved using the methods of Guo [14] and Ladd and Verberg [19].

(2) ϕ_i is refined by more careful definition of the interface.

(3) A higher-order accurate calculation of numerical derivatives in ϕ_i is used.

(4) A kinematic condition is introduced.

A. Interface source term ϕ_i

A constant source term $\phi_i = 3t_p\mathbf{G}\cdot\mathbf{c}_i$ is a well-known device for inserting a constant gradient $\mathbf{G}$. It is recognized that spatial dependence in ϕ_i requires a modified Chapman-Enskog analysis of the macroscopic dynamics [14,17]. The method of Guo is a progression of earlier work, in particular of Ladd and Verberg [19]. It may be used to yield an expression for a source term in terms of the target, space-dependent macroscopic force $\mathbf{F}(\mathbf{r})$ [14]:

$$\phi_i(\mathbf{r}) \equiv t_p\left(1 - \frac{1}{2\tau}\right)[3(\mathbf{c}_i - \mathbf{u}^*) + 9(\mathbf{c}_i \cdot \mathbf{u}^*)\mathbf{c}_i] \cdot \mathbf{F}(\mathbf{r}),$$

$$\qquad (14)$$

where

$$\mathbf{u}^* \equiv \frac{1}{\rho}\left(\sum_i f_i\mathbf{c}_i + \frac{1}{2}\mathbf{F}(\mathbf{r})\right). \qquad (15)$$

Equation (14) replaces that given in Eq. (13); Eq. (15) gives an accompanying redefinition of the model's velocity. Note that Eq. (14) remains correct if the macroscopic force also contains time dependence. The Navier-Stokes equation (7) now acquires position dependence in the body-force term,

$$\frac{\partial}{\partial t}\rho u_\alpha^* + \frac{\partial}{\partial x_\beta}\rho u_\beta^* u_\alpha^* = -\frac{\partial}{\partial x_\alpha}\rho + \frac{\partial}{\partial x_\beta}\frac{\partial}{\partial x_\beta}(2\rho\nu S_{\alpha\beta}^*) + \mathbf{F}_\alpha(\mathbf{r}).$$

$$\qquad (16)$$

Note also that the right-hand side of Eq. (14) reduces to the right-hand side of Eq. (13) for $\mathbf{u}^* \rightarrow 0$ and $\tau \rightarrow 1$.

In addition to requiring a redefined velocity, Guo's method removes the local relationship between the fluid strain rate and the distribution function, $f_i^{(1)}$ [14], the usual form of which is reproduced in Eq. (32), Sec. V C. For some applications this is unfortunate; Ladd points out that local expressions for the strain rate are advantageous when calculating, for example, stresses imparted onto Lagrangian particles suspended in the LB fluid [20]. The approach of Ladd and Verberg [19] for time-independent body forces, applied to our case of an interface force, yields

$$\phi_i(\mathbf{r}) \equiv t_p\left\{3\left[\mathbf{c}_i - \left(1 - \frac{1}{2\tau}\right)\mathbf{u}\right] + 9\left(1 - \frac{1}{2\tau}\right)(\mathbf{c}_i \cdot \mathbf{u})\mathbf{c}_i\right\} \cdot \mathbf{F}(\mathbf{r}),$$

$$\qquad (17)$$

which recovers the Navier-Stokes equations (16) to the accuracy of the method of Guo. However, the continuity equation now acquires an additional term [14],

$$\frac{\partial\rho}{\partial t} + \frac{\partial}{\partial x_\beta}\rho u_\beta = -\frac{1}{2}\frac{\partial}{\partial x_\beta}\mathbf{F}_\beta(\mathbf{r}). \qquad (18)$$

This approach, referred to in Ref. [14] as method 2a, requires no redefinition of velocity, and represents (in our opinion) an

TABLE II. Summary of (i) the normalized steady-state transverse position y/L_y and (ii) the normalized steady-state velocity u_d/U_0 for neutrally buoyant drops, the initial radius is 15 lattice units, exposed to a uniform shear flow of characteristic shear velocity U_0.

$1/\tau$	ν	Re	Re$_d$	Ca	y/L_y ±0.01	U_d/U_0 ±0.01	δy	$\delta y'$	$\delta y''$
0.85	0.23	1.11	0.10	2.98	0.49	0.49	0.45	1.92	1.93
0.90	0.20	1.23	0.11	2.70	0.48	0.48	0.78	1.72	1.72
0.95	0.18	1.36	0.12	2.43	0.49	0.48	0.61	1.54	1.54
1.00	0.17	1.50	0.16	2.21	0.51	0.51	0.49	1.12	1.12
1.05	0.15	1.66	0.15	1.99	0.49	0.48	0.43	1.35	1.35
1.10	0.14	1.83	0.17	1.80	0.50	0.50	0.59	1.91	1.81
1.15	0.12	2.03	0.18	1.63	0.50	0.50	0.19	3.25	5.20

optimum treatment of variable forcing without recourse to a redefined velocity. However, when using method 2a for a spatially varying force, the continuity equation acquires nonphysical terms. The latter may, in fairness, be small and in certain applications, an intact interpretation of velocity may outweigh this disadvantage. For present purposes however, method 2a may be expected to produce inferior results owing to this continuity equation effect.

Equations (14) and (17) together with Eq. (15) (where appropriate) represent expressions for $\phi_i(\mathbf{r})$ each of which is an improvement upon our original expression in Eq. (13). We compare results from both methods in Table II; everywhere else we use Eq. (14).

B. Interface definition and cumulative forcing

The criterion for inclusion of ϕ_i in evolution equation (4) is modified to a condition on the gradient of ρ^N. We now include ϕ_i if $|\nabla \rho^N| < 10^{-8}$. With $O(4)$ numerics (see Sec. IV C), this distributes the interface forcing for a more accurate cumulative effect. Meanwhile, numerical segregation ensures that the length scale of the variation in ρ_N is unaffected. We choose to use the internal (say) red relaxation parameter $\tau = \tau_R$ only when $\rho^N(\mathbf{r}, t) > 0.99$; this follows a level-set philosophy and places the interface entirely
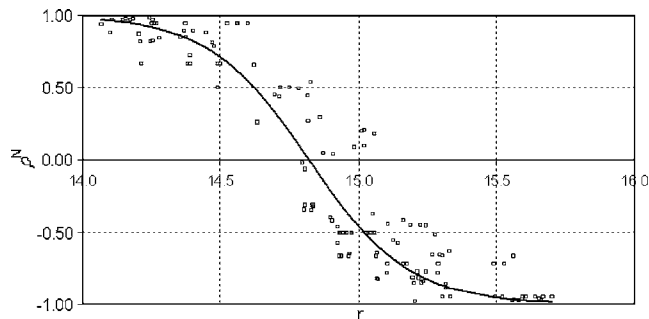
FIG. 3. The distribution of phase field index for a neutrally buoyant red drop ($\rho^N = +1$) at rest, suspended in a blue fluid ($\rho^N = -1$). Both fluids have collision parameter $\tau = 1$. The initial radius of the drop is 15 lattice units, the interfacial region has a characteristic width of about a single lattice unit. The solid line corresponds to a tanh profile fit (see text).

within the embedding fluid. It has the effect of sharpening the phase field boundary and the location of any viscosity change.

Figure 3 shows the value of ρ_N versus radial distance for a static drop of initial radius 15 lattice units. The component index, ρ^N, changes essentially over a distance of one lattice unit. The solid line in Fig. 3 corresponds to the function $\tanh[k(r - r_0)]$, with r_0 the average radius of the drop. Least-squares fitted values of $k = 2.77$ and $r_0 = 14.82$ were determined. The collapse of all interface data onto this single contour strongly supports the view that (i) while very narrow, the interface in our modified model has a structure independent of its orientation relative to the underlying lattice and (ii) the drop is isotropic.

Suppose the interface forms a sharp, closed contour in a plane. From the definition of curvature it can be shown that the line integral, along this contour, of a normally directed force, proportional in magnitude to local contour curvature, K, must vanish. However, numerical derivatives introduce inaccuracies in K; a nonzero value of this line integral results. Therefore, we record the small, fluctuating but nonzero, *total* applied interface force and eliminate any imbalance by applying its negative over the interface region, weighted by the magnitude of local interface force. The corresponding correction to the source term of Eq. (14) at position $\mathbf{r}$ is

$$\delta \phi_i \equiv -3t_p \left(\frac{\sum_{\mathbf{r}'} \mathbf{F}(\mathbf{r}') \cdot \mathbf{c}_i}{\sum_{\mathbf{r}'} |\mathbf{F}(\mathbf{r}')|} \right) |\mathbf{F}(\mathbf{r})|, \qquad (19)$$

where the summation on $\mathbf{r}'$ runs over all points in the interface region.

To police the cumulative interface force it may seem reasonable to determine some form of local curvature average. However, sharp, local fluctuations in K are actually necessary to keep an interface sharp and smooth. Consider Fig. 4 in which interface sites with $-0.9 < \rho^N < 0.9$ have the direction of their color gradient displayed. As the tangent to the local interface direction approaches a lattice direction local curvature K changes sign as follows. Point (103,82) in Fig. 4 lies in a region above a vertical length of interface, tangent to line $x = 106$. For a circular drop, the interface must, near to
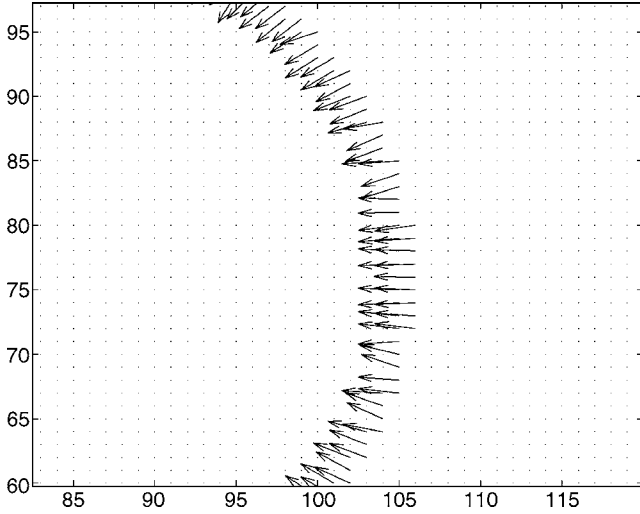
FIG. 4. Detail of the normalized color gradient field for a rest drop. Point (103,82) lies in a region above a vertical length of interface tangent to line $x=106$. In order to have an overall isotropic, circular drop the interface must switch to a parallel line of nodes. Near (104,82), the interface switches onto another, parallel line of nodes $x=105$. When this happens the local curvature must fluctuate and change sign.

position (103,82), switch and continue on another, parallel line $x=105$. When this happens the local curvature must fluctuate and even change sign. Local smoothing undermines this curvature elimination property of the algorithm, thereby undermining the mechanism by which the interface is kept smooth and sharp.

C. Calculation of numerical derivatives

The internode links $\mathbf{c}_i$, corresponding weights t_p, and indexing of the D2Q9 [16] lattice are defined in Table I. Note the implicit use of unit lattice spacing. By direct calculation this set of lattice link vectors and weights may be shown to have the following even moments:

$$\sum_i t_p = 1,$$

$$\sum_i t_p c_{i\alpha} c_{i\beta} = \frac{1}{3} \delta_{\alpha\beta},$$

$$\sum_i t_p c_{i\alpha} c_{i\beta} c_{i\gamma} c_{i\delta} = \frac{1}{9} (\delta_{\alpha\beta}\delta_{\gamma\delta} + \delta_{\alpha\gamma}\delta_{\beta\delta} + \delta_{\alpha\delta}\delta_{\beta\gamma}), \quad (20)$$

while the corresponding odd moments are zero.

Now, a Taylor expansion of the function $\phi(\mathbf{r}+N\mathbf{c}_i)$, about $\mathbf{r}$, may be approximated,

$$\phi(\mathbf{r} + N\mathbf{c}_i) \simeq \phi(\mathbf{r}) + \sum_{n \leq n_0} \frac{1}{n!} N^n (\mathbf{c}_i \cdot \nabla)^n \phi(\mathbf{r}), \quad (21)$$

where $N=1,2,3,\ldots$. Retaining derivatives to $O(n_0)$ yields an expression with order of accuracy n_0 in lattice spacing. Multiplying Eq. (21) by the product $t_p c_{i\alpha}$ ($\alpha=x,y$), summing the

result upon link index i and appealing to the moment properties in Eqs. (20), one can obtain a system of simultaneous equations, with spatial derivatives such as $\partial^2 \phi(\mathbf{r})/\partial x \partial y$ as its independent variables. The equations in this system are characterized by the choice of parameter α and the value of range parameter N. Taking $n_0=3$ and $N \leq 3$ one can solve this system for $O(n_0+1=4)$ accurate expressions for the first spatial derivatives of $\phi(\mathbf{r})$,

$$\nabla \phi(\mathbf{r}) = \sum_i t_p \left(\frac{9}{2} \phi(\mathbf{r} + \mathbf{c}_i) - \frac{9}{10} \phi(\mathbf{r} + 2\mathbf{c}_i) + \frac{1}{10} \phi(\mathbf{r} + 3\mathbf{c}_i) \right) \mathbf{c}_i.$$

$$(22)$$

Clearly this method of calculating gradients undermines that locality of the algorithm which is considered to be one of the strengths of LB. However, the additional overhead introduced only scales as the total length of interface in the simulation.

D. Kinematic condition

We state the kinematic condition as the requirement that the internal and external fluids have the same velocity at the interface. In fact the kinematic condition is important in multicomponent flow. The Re=0 calculation of flow past a spherical drop demonstrates this very clearly [21]. Here we present a method of coupling the dynamics of the phase field and those of the fluid, aiming to embed a kinematic condition. Throughout Sec. IV D the asterisk superscripts are discrete positions, point (x^*, y^*) is a discrete lattice position, (x, y) is a sublattice point.

The narrow interfaces generated by the methods considered here correspond, typically, to local interface profiles with only one node on the lattice with $|\rho^N(x^*, y^*, t^*)| < 0.8$. Take sublattice contour $\rho^N(x, y)=0$ to define the (off-lattice) center of the interface, suppose that all the N (M) points $\{(x_i^*, y_i); i=1,\ldots,N\}$ ($\{(x_i, y_i^*); i=1,\ldots,M\}$) at which this contour intersects the short lattice links have been determined (by searching vertically and horizontally over the lattice and using linear interpolation). Contour $\rho^N(x, y)=0$ bounds what should be two different fluid domains; boundary and, ideally, kinematic conditions should apply between the bulk fluids on this contour. $\{(x_i^*, y_i); i=1,\ldots,N\}$ $\cup \{(x_i, y_i^*); i=1,\ldots,M\}$ is a suitable set of points upon which to apply appropriate conditions. Of course, this choice of a set of points implicitly defines a sharp interface.

Noting that the dynamic boundary conditions on interfacial stress are implicit in our core method [10], and aiming to preserve resolution and to conserve local momentum, we consider three practical approaches to a kinematic condition, each based upon the set of points $\{(x_i^*, y_i); i=1,\ldots,N\} \cup \{(x_i, y_i^*); i=1,\ldots,M\}$.

Method 1: Take the two sets of pairs of points $\{([x_i^*, \text{int}(y_i)+1], [x_i^*, \text{int}(y_i)-1]); i=1,\ldots,N\}$ and $\{([\text{int}(x_i)+1, y_i], [\text{int}(x_i)-1, y_i]); i=1,\ldots,M\}$, where $\underline{\text{int}}(x_i)$ denotes the integer part of x_i. Find the mean velocity $\overline{\mathbf{u}}^*$ of each such pair of points,

$$\overline{\mathbf{u}^*} = \frac{\rho[\text{int}(x_i)+1, y_i]\mathbf{u}[\text{int}(x_i)+1, y_i] + \rho[\text{int}(x_i)-1, y_i]\mathbf{u}[\text{int}(x_i)-1, y_i]}{\rho[\text{int}(x_i)+1, y_i] + \rho[\text{int}(x_i)-1, y_i]},\tag{23}$$

and assign the precollision fluid velocity at points $[x_i^*, \text{int}(y_i)+1]$ and $[x_i^*, \text{int}(y_i)-1]$ to $\overline{\mathbf{u}^*}$; it is velocity $\overline{\mathbf{u}^*}$ which is used to evaluate the equilibrium distribution $f_i^{(0)}(\rho, \overline{u^*})$ in Eq. (4). Fluid just inside each of the separated components is thus induced to move at the same speed. It is important to note that it is the modified velocity, defined in Eq. (15), which is averaged.

Method 2: Determine the mean, velocity $\overline{\mathbf{u}^{*\prime}}$ in an interfacial neighborhood $[\text{int}(x_i)-1] \leq x^* \leq [\text{int}(x_i)+1], [\text{int}(y_i)-1] \leq y^* \leq [\text{int}(y_i)-1]$,

$$\overline{\mathbf{u}^{*\prime}} = \frac{\sum_{i=-1,0,1}\sum_{j=-1,0,1}\rho(x^*+i, y^*+j)\mathbf{u}(x^*+i, y^*+j)}{\sum_{i=-1,0,1}\sum_{j=-1,0,1}\rho(x^*+i, y^*+j)}.\tag{24}$$

As in method 1, all nodes in this region are then evolved according to Eq. (4) with an equilibrium distribution $f^{(0)}(\rho, \mathbf{u}^{*\prime})$. Clearly this method results in a loss of resolution in the interface region relative to method 1.

Method 3: Using an alternative, nonnumerical method for component segregation [22,23] with segregation parameter $\beta=0.7$ (notation of Ref. [23]) follow method 1 above. Method 3 therefore has a distributed interface of much greater width than those obtained by the numerical segregation otherwise considered; with $\beta=0.7$ the value of ρ_N switches between -1 and $+1$ in the surface normal direction over six lattice spacings (rather than one lattice spacing with numerical segregation shown in Fig. 3). One advantage of a diffuse phase boundary is that the contour $\rho^N(x,y)=0$ is better defined. It is necessary briefly to introduce this additional segregation algorithm variant in order to obtain a contextual view of the kinematic condition.

V. RESULTS AND DISCUSSION

There is a considerable body of literature relating to the transverse migration or lift of a solid particle subject to simple shear or parabolic flow. Lift is widely discussed in the context of a range of important applications such as resuspension. The term lift may suggest a direction of motion dictated by a gravitational field; however it is important to note that the effect is simply the migration of a particle or droplet in a flow as a consequence of a hydrodynamic interaction of the particle with one or more neighboring boundaries. The direction of migration is determined by the nature of the flow and the boundaries. As a basis for evaluating our model we consider the lift of a deformable, incompressible, neutrally buoyant liquid drop in simple shear flow, at low Re_d, with a capillary number $\text{Ca} \sim 2$ which permits only restricted deformation.

The chosen geometry is a stringent test of our algorithm. For one thing, anticipating our results, lift appears to rely

upon a small imbalance of hydrostatic pressure. To this the interface algorithm must be sensitive. Second, for a small shear rate, a drop's drift velocity component in the direction of the unperturbed shear gradient is small, particularly as the drop approaches its steady-state position. Any lack of Galilean invariance is thus exposed in the transverse component of the motion.

A. Simulations of drop lift in shear flow

It is important to use accurate boundary conditions. The necessary Dirichlet boundary conditions cannot be represented by popular LB methods like on-link or midlink bounce back [12]. To impose the $O(2)$ accurate velocity boundary conditions, the method reported in Ref. [24] was used. By $O(2)$ accurate we mean (i) second-order accurate in lattice spacing *and* (ii) able correctly to construct boundary distributions f_i up to the level denoted $f_i^{(2)}$ [12].

Advection and lift tests identical to those described in Sec. II were repeated using all four innovations described in Sec. IV and an $O(2)$ accurate lattice closure scheme to impose velocity boundary conditions. In particular, the kinematic condition reported in method 1 of Sec. IV D was used. In terms of the results in Fig. 2, simple Galilean invariance is restored down to values of parameter $U_0/\alpha \sim 0.003$. This modest improvement (compared with the data of Fig. 2) is to be expected from the arguments we set out in Sec. V C.

Lift tests were conducted on a drop of initial radius 15 lattice units, placed on a $L_x \times L_y = 150 \times 50$ lattice, bounded by Dirichlet velocity conditions in the y direction and periodic boundary conditions in the x direction. This, of course, produced an infinite line of drops. The drop was positioned with its center at $y=20$ lattice units and equilibrated for $5 \times 10^3 \leq t$ time steps. For time steps in the range $5 \times 10^3 \leq t \leq 4 \times 10^5$ the $y=\{L_y, 0\}$ boundary was set to move with x-velocity $\{5 \times 10^{-3}, 0\}$ lattice units per time step, respectively. What would, for a uniform system, be a shear profile $u_x=(U_0/L_y)y$ was thus applied to stable drops.

We denote the center of mass y coordinate of the drop by y_0 and the x and y components of its velocity by u_d and v_d, respectively. Mechanical equilibrium or steady state is defined by a vanishing long-time average $\langle v_d \rangle_t = 0$. At steady state, general arguments require the center of mass (x_0, y_0) of a neutrally buoyant drop to advect at velocity $(U_d, V_d)=(U_0/2, 0)$ at y position $L_y/2$. Results for $(\langle u_d \rangle_t, \langle v_t \rangle_t)$ from the simulation can therefore be compared with expected values $(U_0/2, 0)$.

For all the results in Figs. 5–8, and Table II, simulation parameters were $\rho=2$, $\dot{\gamma}=10^{-4}$, $\alpha \sim 3.4 \times 10^{-3}$. All data presented assume that the drop liquid and the embedding fluid have the same viscosity. The single LB relaxation parameter τ was varied over a range $0.85 \leq 1/\tau \leq 1.15$. Steady-state
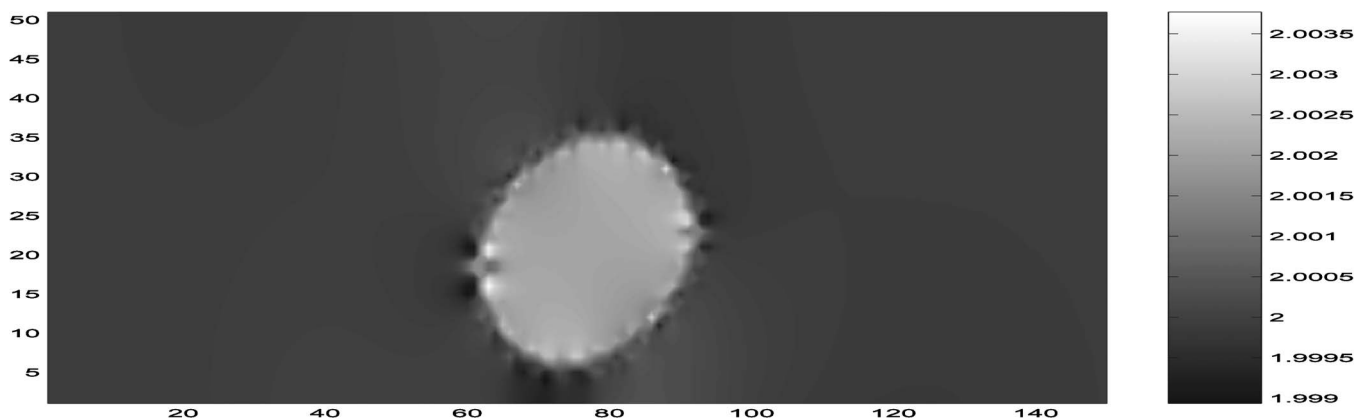
FIG. 5. The pressure distribution for a droplet at the point at which transverse migration commences. Note the fluctuation in the pressure near to the interface.

data are presented for $0.100 \leq Re_d \leq 0.165$ and $2.98 \leq Ca \leq 1.63$. The *channel* Reynolds number ranges in our data $1 \leq Re \leq 2$ (see Table II for exact values).

Figures 5 and 6 are an abbreviated life history of a lifting drop. Figure 5 shows the partially deformed and orientated drop at the point at which transverse migration commenced, depicted using pressure $P \equiv \rho/3$ (for our model). Note the high pressure region visible between the drop and the closest, rest boundary. From these and similar images it is apparent that substantial drop deformation and orientation occur before any lift commences. Figure 6 shows the corresponding, now symmetric, pressure distribution about the drop at steady state. Both Figs. 5 and 6 show fluctuations in pressure in the interfacial region; the phase field, ρ^N, by contrast, varies smoothly across the interface (Fig. 3).

More data are shown in Table II and Fig. 7. Values of y_0/L_y and normalized final advection velocities U_d/U_0 are recorded in Table II. The last three columns of Table II compare δy, the absolute difference $|y_0 - L_y/2|$ with $\delta y'$, the corresponding data obtained with the method of Ladd and Verberg [19] [Eq. (17)] and $\delta y''$ obtained by using our unmodified algorithm [10] [Eq. (13)]. Notwithstanding a need to adjust the velocity, the method based upon Guo's analysis [14] outperforms the others. A typical drop center-of-mass trajectory is shown in Fig. 7. Note, however, that the

Ladd-Verberg approach is not at its best in this application, and its unadjusted velocity may well represent an advantage in other applications. Figure 8 shows data for all the trajectories of all the drops in Table II. Their y excursion is plotted against the corresponding x velocity, sampled every 2.0×10^5 time steps. Point $y=25$, $U_d=2.5 \times 10^{-3}$ is the equilibrium position required by general Galilean invariance. All data lie on the same trajectory.

A measure of the Gallilean invariance of the current algorithm is the steady-state value of distance from midchannel, δy. Outside our range of parameter it begins to fail. However, an improved performance in terms of consistency is clear from a comparison of the last two columns of Table II. From the sixth row, for $Ca/Re \sim 1$, $Ca/Re_d \sim 10$, the current model has 28% of the error of the unmodified model of Ref. [10]; over the range of data in Table II, the error in the current (unmodified) algorithm, measured by δy ($\delta y'$), is 0.51 (2.10). With $\delta y \leq 0.5$ as the criterion, $Ca/Re_d \sim 0.78$ are possible with the modified algorithm.

B. Kinematic condition

To illustrate the kinematic condition outlined in Sec. IV D, consider the relative normal velocity in the region of the interface. At steady state, the deformation of a sheared
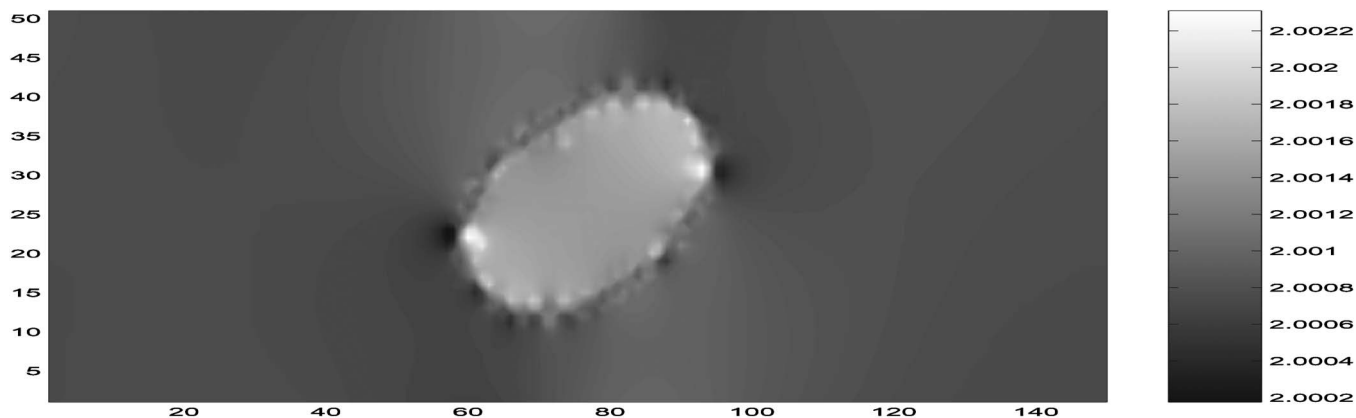
FIG. 6. The pressure distribution for the same droplet at steady state. Note the small regions of high pressure located at the tips. Some slight faceting is visible in this image.
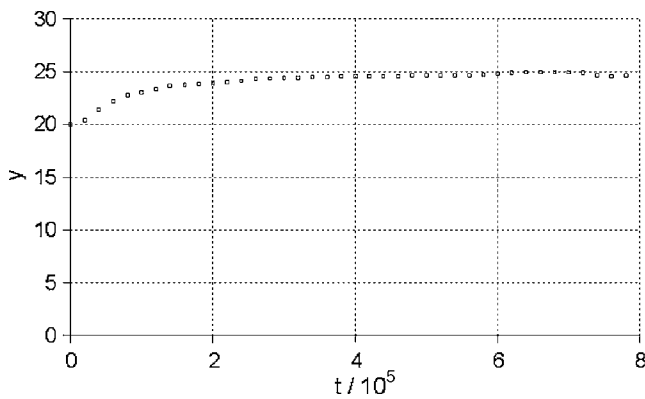
FIG. 7. y positions and x velocities for all the trajectories of all the drops in Table II. y excursion is plotted against the corresponding x velocity, sampled every 2.0×10^5 time steps. Point $y=25$, $U_d=2.5 \times 10^{-3}$ is the equilibrium position required by general Galilean invariance.

drop is constant. The component of fluid velocity relative to the drop in the direction of the interfacial normal, u_n, must vanish and the drop interface should correspond to a closed contour $u_n=0$. The interface normal is readily obtained from the (negative of) direction of $\nabla \rho^N$. The constant center-of-mass velocity, $\mathbf{U_d}$, of a drop was calculated and subtracted from the steady-state velocity field to allow u_n to be calculated,

$$u_n = (u_x - U_{dx}) \left(\frac{-\frac{\partial \rho^N}{\partial x}}{|\nabla \rho^N|} \right) + (u_y - U_{dy}) \left(\frac{-\frac{\partial \rho^N}{\partial y}}{|\nabla \rho^N|} \right). \quad (25)$$

Note that $U_d/U_0=0.5$ in the channel center, on general grounds.

Figures 9 and 10 each show the $u_n=0$ contour. Both images correspond to Ca=2.5, Re$_d$=0.13. Figure 9 corresponds to the three cases of (a) no kinematic condition, (b) the kinematic condition of method 1 and (c) the kinematic condition method 2; Fig. 10 corresponds to method 3.
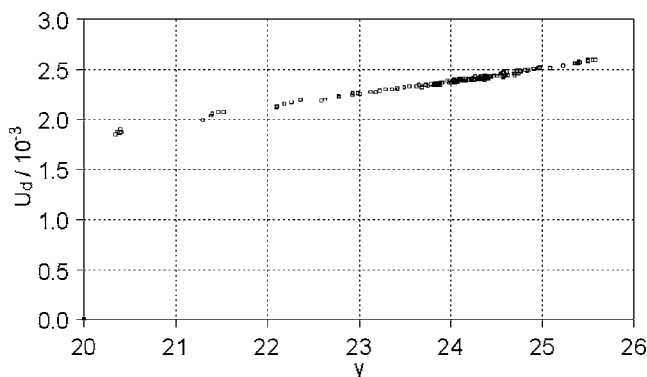
FIG. 8. Center-of-mass drop trajectory. Note that all the drops in the study appear to have a trajectory broadly indistinguishable from that shown here. For times in excess of the $7.0e5$ time steps the drop remains at the channel center position $y=25$. Note also that a degree of pinning is apparent as the drop approaches its steady-state position.
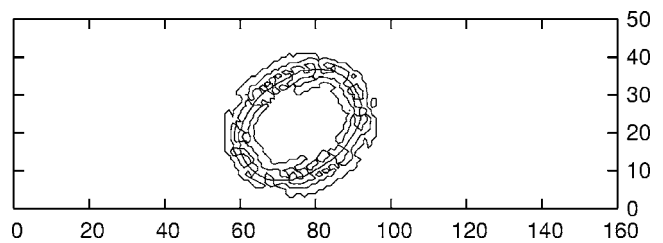
FIG. 9. Ca=2.5, Re$_d$=0.13. Data for numerical segregation with (a) kinematic conditions of method 1 (b) kinematic condition of method 2 and (c) no kinematic condition [all (a)–(c) produce results with no differences visible to the eye]. The fluctuating solid contour corresponds to zero surface normal velocity, $u_n=0$ [see Eq. (25)]. The interface, $\rho^N=0$, corresponds to the axis of the toroidal region covered by this fluctuating solid contour.

For no kinematic condition (Fig. 9), the fact that the u_n=0 contour is so fragmented, relative to the $\rho^N=0$ contour, demonstrates that, despite a sharp phase field boundary, the hydrodynamic boundary is diffuse. It may be hoped that a kinematic condition would produce better correlation between the u_n=0 and the interface. Unfortunately data corresponding to methods 1 and 2 of Sec. IV D show no improvement observable to the eye. Figure 10, which, recall, corresponds to a model extension, shows a large improvement both in terms of an identifiable u_n=0 contour and its correlation with the contour $\rho^N=0$, albeit for a more diffuse interface. In respect of the latter, however, it is important to note that the noise in the u_n=0 contour, clear in Fig. 9, extends over approximately six lattice sites in the normal direction; in this sense the hydrodynamic boundary between the fluids is approximately as diffuse (but rather more noisy) as the phase field boundary generated by the modified segregation represented in Fig. 10.

The fact that the modified segregation of Fig. 10 shows a u_n=0 contour which is not closed, for example, at the poles of the drop is an artifact. Around the poles, flow is directed
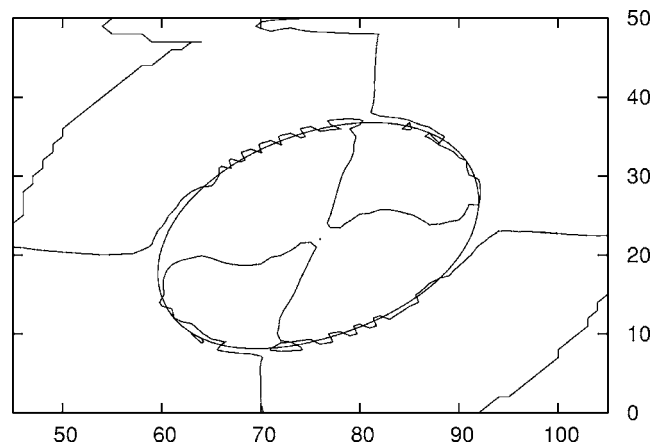
FIG. 10. Kinematic condition of method 3, Sec. IV D used. Ca=2.5, Re$_d$=0.13. Overlaid contours of $\rho^N=0$ (closed ellipsoid) and $u_n=0$. The correlation between the phase field and hydrodynamics information in this simulation is clearly much improved. Note that the two diagonal lines extending from (92,0) to (105,14) and (45,24) to (70,50) are artifacts of the way in which this information was compiled.

along the tangent to the interface and the normal component of velocity is very small throughout finite polar regions. It is the boundary to these regions which the $u_n=0$ contour follows. Hence, with the modified segregation of method 3, Sec. IV D, the correlation between hydrodynamic boundary and phase boundary $\rho^N=0$ is good over whole interface.

C. Discussion

We discuss issues relating to the LB simulation, reserving for Sec. VI our remarks on the lift. Unless otherwise stated, suppose that the original model (Ref. [10]) is in use.

Eventual loss of simple Galilean invariance seems universal in multicomponent LB on the following approximate argument. Consider a two-dimensional D2Q9 LB fluid. Suppose the lattice fluid is translating uniformly at velocity $\mathbf{U_0}=U_0\hat{e}_x$. It is then described everywhere by an equilibrium distribution function $f_i^{(0)}(\rho,\mathbf{U_0})$; e.g., Eq. (6). The momentum distribution for a link j, parallel with imposed flow, is thus shifted about its rest equilibrium value (of $t_p\rho$) by an amount

$$df_j = 3t_p\rho U_0 + O(U_0^2). \tag{26}$$

Note, the numerical factor 3 in Eq. (26) has dimensions which give the overall expression for df_j units of ρ. Now, suppose the LB fluid contains an embedded drop, radius R. When the interface-inducing source term ϕ_j [Eqs. (4) and (13)], competes with df_j, information relating to the advection of the interface is lost. This leads to an approximate, $O(U_0^2)$ accurate, condition for loss of flow information in the interface region,

$$3t_p\rho U_0 \geq \frac{3}{2}\frac{\alpha}{R}t_p\frac{\partial}{\partial x}\rho^N, \tag{27}$$

where, recall, the factor $\frac{3}{2}$ is dimensional. Taking a value for the phase field gradient of unity (typical of the center of the interface) and $R=15$, we obtain

$$\frac{U_0}{\alpha} \geq \frac{1}{2}\frac{1}{\rho R} = \frac{1}{2 \times 15 \times 2.0} \approx 0.035, \tag{28}$$

where we have substituted the value of $\rho=2.0$ used for all our results.

Given the approximate nature of these arguments, the prediction in Eq. (28) is very well supported by the simulation results shown in Fig. 2; a fit to the data (solid line, Fig. 2) gives a figure of 0.049. We note that, using our modified forcing, defined in Eq. (14) or, indeed an alternative form of LB interface generating algorithm, the central assumptions of the above analysis survive.

Similar arguments apply to the problem of a drop subject to fluid stresses. The lift simulations reported in Sec. V consider a drop suspended in a uniform applied shear,

$$u_\alpha = e_{\alpha\beta}x_\beta, \quad e_{11} = e_{21} = e_{22} = 0, \quad e_{12} = \dot{\gamma}, \tag{29}$$

which we take to be the unperturbed flow. There is an exact solution for the f_i's in this flow [25], for our model it may be written [26] as

$$f_i = f_i^{(0)}(\rho,\mathbf{u}) - \pi t_p\frac{\rho e_{\alpha\beta}Q_{\alpha\beta}}{bc_s^2}, \quad Q_{\alpha\beta} \equiv \left(c_{i\alpha}c_{i\beta} - \frac{1}{3}\delta_{\alpha\beta}\right). \tag{30}$$

We note in passing that our unit time step, introduced from Eq. (4), actually multiplies the second term on the right-hand side of this equation (see the Chapman-Enskog derivation [12] of Hou *et al.* [27]) giving that term the overall dimensions of density. For our underlying D2Q9 model, the number of velocities $b=2$ and $c_s^2=1/3$ (in units of lattice velocity squared), so Eq. (30) implies an expression for the so-called $f^{(1)}$ component (see e.g., Ref. [12] and Hou *et al.* [27]) of the momentum distribution function

$$f_i^{(1)} = -t_p\frac{3\tau\rho}{2}\dot{\gamma}c_{ix}c_{iy}, \tag{31}$$

in which, note, the factor 3 has units which cancel those of the factor $c_{ix}c_{iy}$, again giving the right-hand side of Eq. (31) dimensions of ρ overall. Now, it is well known that the strain rate in single-component LB fluids is given by $S_{\alpha\beta}=-(3/2\rho\tau)\Sigma_i f_i^{(1)}c_{i\alpha}c_{i\beta}$ from which it is possible to show that the viscous stress is controlled by the $f_i^{(1)}$'s,

$$\sigma'_{\alpha\beta} = \frac{1}{4}\left(\frac{1}{\tau} - 2\right)\sum_i f_i^{(1)}c_{i\alpha}c_{i\beta}, \tag{32}$$

and that the LBGK evolution equation (4) can, with the assumptions of the original model of Ref. [10], be written in terms of the $f_i^{(1)}$'s [12]:

$$f_i(\mathbf{r} + \mathbf{c}_i, t + 1) = f_i^0(\rho, \rho\mathbf{u}) + \left(1 - \frac{1}{\tau}\right)f_i^{(1)} + \phi_i. \tag{33}$$

Suppose now that the LB fluid contains a drop, radius R, under shear. It is the fluid stresses in the interfacial region which impress force between the drop and embedding fluid. Clearly, from Eq. (32), this stress is determined by the $f_i^{(1)}$'s So if the interface-inducing source term ϕ_i competes with $f_i^{(1)}$, information relating to the fluid stress distribution about the interface is degraded. Hence we characterize loss of stress information, or lift, by

$$\phi_i \approx f_i^{(1)}. \tag{34}$$

Substituting from Eqs. (13) and (31) into Eq. (34), canceling the (dimensional) numerical factors and t_p, we find a simple condition for degradation of surface stress information:

$$\frac{\rho\tau\dot{\gamma}R}{\alpha|\nabla\rho^N|} \approx 1. \tag{35}$$

Thus, taking the parameters used for the data of Table II, $\tau \sim 1$, $\rho=2$, and $\dot{\gamma}=10^{-4}$ and taking $|\nabla\rho^N| \sim 1$, Eq. (35) suggests an upper limit of surface tension $\alpha \sim 3 \times 10^{-3}$. This value accords with observations. In Table II, recorded values of $\delta y'$ show that the drops with a value of $\alpha=2.5 \times 10^{-3}$ used there are not forced into the position required by general Galilean invariance. However, the results presented in Table II for δy, using the improved model (for the same parameters) reflect a simulation with considerably improved gen-

eral Galilean invariance. We believe this is due, in part, to the use of the analysis of Guo *et al.* [14], which ensures that the background fluid stress information is less corrupted by the interface forcing.

VI. CONCLUSION

We have presented a two-component lattice Boltzmann model of flow, designed to be efficient in the continuum approximation and to support essentially unstructured interfaces. It contains a set of modifications to our preceding model of Ref. [10], described in Sec. IV. In outline, these modifications achieve improved fluid-fluid interface behavior in terms of drop shape (faceting) at smaller capillarity number, Ca, and Reynolds numbers Re and Re$_d$. These improvements in the basic reliability of this class of LB model make it more suitable for microfluidic and non-Brownian colloid applications, e.g., those in Refs. [1,2], in which local Re$_d$ variations must occur. The approximate analysis of Sec. V C suggests that the new method achieves better results by improving the representation of stress near the interface.

We have used our improved model to report on 2D simulations of lift on slightly deforming, neutrally buoyant, immiscible liquid drops in simple shear. Clearly, on general grounds, a drop must migrate across stream lines of the undisturbed simple shear flow, until it reaches a position of

mechanical steady state: which is what we observed. Accurately to use LB one must be confident that any small pressure fluctuations can register stresses in the interfacial region of the fluids, where pressure was seen to be fluctuating due to interfacial forcing; a point underscored in Figs. 5 and 6, in which the relative size of the lift-inducing pressure difference and the interfacial pressure jump are made clear.

It is worth commenting that results also demonstrate that transverse position and drop velocity increase in proportion; also a marked degree of deformation and orientation in local flow precedes any lateral migration. This, again, is an unsurprising observation given uniform nature of applied shear. It is also worth repeating that the migration trajectory information shown in Figs. 8 and 7 was not observed significantly to vary over all drops in this study.

Very small values of Ca and Re$_d$ remain elusive. This regime might be achieved by reducing local shear rates $\dot{\gamma}$. From Eq. (35), this can be balanced only by a reduction in the value of phase field gradient $\nabla \rho^N$. Taken with the results of Figs. 9 and 10, this observation calls into question the practical utility of a sharp phase boundary close to which the velocity, in particular, fluctuates. The results in Fig. 10 are important in this respect. Figure 10 depicts a distributed interface algorithm but the velocity field correlation with a particular value of phase field is greatly improved, actually making the hydrodynamic boundary sharper.

[1] M. M. Dupin, I. Halliday, and C. M. Care, J. Phys. A **36**, 8517 (2003).

[2] M. M. Dupin, I. Halliday, and C. M. Care, Philos. Trans. R. Soc. London, Ser. A **362**, 1885 (2004).

[3] S. Jadhav, C. D. Eggleton, and K. Konstantopoulos, Biophys. J. **88**, 96 (2005).

[4] A. Esmaeeli and G. Tryggvason, J. Fluid Mech. **377**, 313 (1998).

[5] K. Sankaranarayanan, I. G. Kevrekidis, S. Sundaresan, J. Lu, and G. Tryggvason, Int. J. Multiphase Flow **29**, 109 (2003).

[6] M. R. Swift, W. R. Osborn, and J. M. Yeomans, Phys. Rev. Lett. **75**, 830 (1995).

[7] X. W. Shan and H. D. Chen, Phys. Rev. E **49**, 2941 (1994).

[8] M. R. Swift, E. Orlandini, W. R. Osborn, and J. M. Yeomans, Phys. Rev. E **54**, 5041 (1996).

[9] A. K. Gunstensen, D. H. Rothman, S. Zaleski, and G. Zanetti, Phys. Rev. A **43**, 4320 (1991).

[10] S. V. Lishchuk, C. M. Care, and I. Halliday, Phys. Rev. E **67**, 036701 (2003).

[11] J. U. Brackbill, D. B. Kothe, and C. Zemach, J. Comput. Phys. **100**, 335 (1992).

[12] S. Succi, *The Lattice Boltzmann Equation for Fluid Mechanics and Beyond* (Oxford/Clarendon, New York, 2001).

[13] M. Do-Quang, E. Aurell, and M. Vergassola, Internal Report 00:03, http://www.psci.kth.se/Activities/Reports/Results/R_2000_03/psci2000_03.pdf

[14] Z. Guo, C. Zheng, and B. Shi, Phys. Rev. E **65**, 046308 (2002).

[15] A. Wagner, Int. J. Mod. Phys. B **17**, 193 (2003).

[16] Y. H. Qian, D. d'Humieres, and P. Lallemand, Europhys. Lett. **17**, 479 (1992).

[17] I. Halliday, L. A. Hammond, C. M. Care, K. Good, and A. Stevens, Phys. Rev. E **64**, 011208 (2001).

[18] I. Halliday, S. P. Thompson, and C. M. Care, Phys. Rev. E **57**, 514 (1998).

[19] A. J. C. Ladd and R. Verberg, J. Stat. Phys. **104**, 1191 (2001).

[20] A. J. C. Ladd, J. Fluid Mech. **271**, 285 (1994).

[21] J. Happel and H. Brenner, *Low Reynolds Number Hydrodynamics* (Nordhof International Publishing, Leyden, 1973).

[22] U. D'Ortona, D. Salin, M. Cieplak, R. B. Rybka, and J. R. Banavar, Phys. Rev. E **51**, 3718 (1995).

[23] M. Latva-Kokko and D. H. Rothman, Phys. Rev. E **71**, 056702 (2005).

[24] I. Halliday, L. A. Hammond, and C. M. Care, J. Phys. A **35**, 157 (2002).

[25] M. Henon, Complex Syst. **1**, 763 (1987).

[26] P. B. Warren, Int. J. Mod. Phys. C **5**, 889 (1997).

[27] S. Hou, Q. Zou, S. Chen, G. Doolen, and A. C. Cogley, J. Comput. Phys. **118**, 329 (1995).